

Research Article

Super Broadband-Sensitive Upconversion in Tm and Ni Codoped Perovskites

Hom Nath Luitel ^{1,2}, Shintaro Mizuno ¹ and Yasuhiko Takeda ¹

¹Toyota Central Research and Development Laboratories, Inc., 41-1, Yokomichi, Nagakute, Aichi 480-1192, Japan

²Amrit Science Campus, Tribhuvan University, Kathmandu, Nepal

Correspondence should be addressed to Hom Nath Luitel; mehomnath@yahoo.com and Yasuhiko Takeda; takeda@mosk.tytlabs.co.jp

Received 30 June 2018; Accepted 25 October 2018; Published 11 February 2019

Academic Editor: Jinn Kong Sheu

Copyright © 2019 Hom Nath Luitel et al. This is an open access article distributed under the Creative Commons Attribution License, which permits unrestricted use, distribution, and reproduction in any medium, provided the original work is properly cited.

We investigated broadband-sensitive upconversion (UC) processes in a series of Tm- and Ni-sensitized ABO_3 ($A = \text{Ca/Sr/Ba}$ and $B = \text{Ti/Zr/Hf}$) perovskites. We have designed combinations of the sensitizers and host cations such that super broad solar radiation ranging from 900 nm to nearly 2000 nm can be efficiently upconverted to 800 nm and shorter wavelengths. The Ni^{2+} ions located at the center of O^{2-} octahedra absorbed photons in the 900–1500 nm range and transferred those energies to the nearby Tm^{3+} ions. The Tm^{3+} ions upconverted those energies at 800 nm, along with the energies absorbed by themselves in the 1100–1250 and 1550–2000 nm ranges, exhibiting super broadband sensitivity. Among the $ABO_3:\text{Tm}, \text{Ni}$ ($A = \text{Ca/Sr/Ba}$ and $B = \text{Ti/Zr/Hf}$) upconverters, $\text{CaTiO}_3:\text{Tm}, \text{Ni}$ exhibited the best performance due to its most distorted crystal structure, which intensified the emission and absorption extents by increasing the optical transition probabilities of Tm^{3+} and Ni^{2+} ions. Introduction of alkali ions at the Ca^{2+} sites and Nb^{5+} ions at the Ti^{4+} sites intensified the UC emission by many folds, mainly due to a charge balance mechanism. At the same time, bigger and smaller codoped alkali ions created an asymmetric crystal field around the active ions and further enhanced the UC emission. Importantly, the upconverted photons are within the absorption edges of GaAs, $\text{Cu}_2\text{ZnSnS}_4$, and dye-sensitized solar cells making wider applications of these upconverters besides crystalline Si solar cells.

1. Introduction

Solar cells, which convert sunlight into a usable form of energy, are the most useful renewable energy devices for the present sustainable society. However, present solar cells suffer severely from their low conversion efficiencies that hardly reach 25% even in the case of optimized single-junction solar cells [1]. The low conversion efficiency is mainly due to the mismatch of photon energies below and above the bandgap of the semiconductor used in solar cell devices. Near-infrared (NIR) photons with energies lower than those of the bandgap of the semiconductor are not absorbed and transmitted whereas photon energies in excess of those of the bandgap of the semiconductor generate heat and are wasted. Photon upconversion (UC), a process of using two or more low-energy photons to generate a high-energy photon, can increase conversion

efficiency of such solar cells. In this technique, an upconverter layer is placed at the back face of a solar cell such that it absorbs low-energy NIR photons transmitted through the solar cell and emits high-energy photons, which are efficiently absorbed by the solar cells.

There are many reports on utilization of such upconverters to increase the efficiencies of solar cells [2–4]. However, conventional upconverters using Er^{3+} -active ions can harvest a narrow solar radiation ranging around 1450–1600 nm and upconvert to 980 nm, mainly useful for crystalline silicon (c-Si) solar cells [5]. There are more reports on using Er^{3+} and Yb^{3+} ions which upconvert 970–1050 nm photons to the visible range, which are mainly applicable to amorphous silicon (a-Si) and dye-sensitized solar cells [6]. Recently, we have reported Ni^{2+} ion-sensitized Er^{3+} upconverters [7–10]. We used six-coordinated Ni^{2+} sensitizers to harvest photons in a range from 1100 to longer than 1400 nm. These energies

are efficiently transferred to the Er^{3+} ions in the Er and Ni codoped systems, followed by Er^{3+} UC emission at 980 nm, in addition to the 1450–1600 nm photons directly absorbed by the Er^{3+} ions. Thus, the combination of Er^{3+} and Ni^{2+} covers a wider solar radiation range from 1100 to 1600 nm and upconverts to 980 nm which is efficiently utilized by c-Si solar cells.

However, this combination of Er^{3+} and Ni^{2+} can only be applied to c-Si solar cells. To further widen the sensitivity range and utilize the concept of harvesting broadband solar radiation in the wider NIR range, here we introduce a new series of upconverters consisting of Tm^{3+} - and Ni^{2+} -active ions that can absorb photons in a 900–2000 nm range and upconvert at 800 nm. Thus, the newly designed Tm^{3+} - and Ni^{2+} -based upconverters can be used to enhance the efficiency of GaAs, $\text{Cu}_2\text{ZnSnS}_4$, a-Si, and some special dye-sensitized solar cells that have absorption edges extended to 800 nm and longer. Besides, such NIR-to-NIR upconverters have potential applications in biomedical imaging and therapies of tumors owing to their biocompatibility, and minimal heating effects as compared to the traditional imaging techniques [11].

2. Experiments

We synthesized ABO_3 (A = Ca/Sr/Ba and B = Ti/Zr/Hf) codoped with Tm^{3+} and Ni^{2+} ions. Other elements like Li⁺ and Nb⁵⁺ were also codoped for charge balance as discussed in our previous Er^{3+} and Ni^{2+} codoped samples [9, 12]. In typical $\text{ABO}_3\text{:Er}$, Li, Ni, Nb samples, Tm^{3+} and Li⁺ ions substitute A sites ions while Ni^{2+} and Nb⁵⁺ ions substitute B site ions. Thus, the compositions were determined like $(\text{Tm}_x\text{Li}_x\text{A}_{1-2x})\text{B}_{1-y-z}\text{Ni}_y\text{Nb}_z\text{O}_3$. However, in our previous $\text{CaTiO}_3\text{:Er}$, Ni upconverters, we realized many folds-intensified UC emission in the Ti-deficit $\text{CaTi}_{0.9}\text{O}_3\text{:Er}$, Ni composition over the stoichiometric and Ti-excess compositions [12]. Thus, here, we prepared similar Ti-deficit $(\text{Ca/Sr/Ba})\text{TiO}_3\text{:Tm}$, Ni compositions. On the other hand, for the other Zr/Hf compounds, off-stoichiometric composition was not good; thus, we prepared stoichiometric compositions. The compound oxide powders were synthesized using component metal-oxide/carbonate powders by the solid-state reaction method. Predetermined amounts of the oxides/carbonates (Kojundo Kagaku, Japan) were well mixed with the help of a small amount of ethanol and then dried at room temperature to evaporate the solvent. Then the dry powders were again mixed and heat-treated at 1300°C for 8 hours in air for reaction and crystallization. Since Ni may exist as a mixed valence, *viz.*, Ni^{2+} and Ni^{3+} , a post-heat treatment at 800°C for 4 hours in N_2 atmosphere was carried out to ensure that all the Ni ions were in the divalent state. Thus, crystalline powders of the target materials consisting of Tm^{3+} and Ni^{2+} were synthesized.

Phase purity and crystalline structure were investigated by XRD using the Cu-K α line and a θ - 2θ method. XRD data for the various samples with different concentrations of the active ions are presented in electronic supplementary information (Figure S1–Figure S4). Irrespective of various dopants and their different concentrations, desired phases were

observed. The detail of such structural analyses was published in our previous reports [8, 9, 12].

For the optical measurements, 0.5 mm thick samples with a sandwich structure of glass/powder/glass were prepared using quartz glass plates. Absorption bands of the Tm^{3+} and Ni^{2+} were investigated by measuring diffuse reflectance spectra of the samples using an integrating sphere. To measure the emission spectra originating from the Tm^{3+} and Ni^{2+} ions, we used semiconductor lasers emitting at 960, 1060, 1180, 1300, 1400, 1490, 1550, and 1660 nm for excitation. An optical parametric amplifier pumped by the third harmonic of Nd-YAG laser with a pulse duration of 7 ns was used for time-resolved measurements of desired emissions.

3. Results and Discussion

Absorption bands of the Tm-only, Ni-only, and Tm- and Ni-doped $\text{CaTi}_{0.9}\text{O}_3$ samples are presented in Figure 1(a). Absorption peaks located at 690, 790, and 1200 nm are originated from the ground state ($^3\text{H}_6$) to the excited state ($^3\text{F}_{2,3}$, $^3\text{H}_4$, and $^3\text{H}_5$, respectively) transitions of the Tm^{3+} ions [13, 14]. A broad absorption band ranging from 1560 to ~2000 nm is assigned to the $^3\text{H}_6$ to $^3\text{F}_4$ transition of Tm^{3+} ions [13]. Other broad absorption bands located at around 550–800 and 900–1500 nm are assigned to the $^3\text{A}_2$ to $^3\text{T}_1$ and $^3\text{A}_2$ to $^3\text{T}_2$ transitions, respectively, of the Ni^{2+} ions [9]. These Ni^{2+} absorption bands are partially overlapped with the Tm^{3+} absorption peaks making the absorption peaks more intense and broad in the Tm and Ni codoped samples and thus cover a broader solar radiation ranging from 900 to 2000 nm. The energy level diagram consisting of Tm^{3+} and Ni^{2+} band positions in the $\text{CaTi}_{0.9}\text{O}_3$ host calculated from the absorption spectra and possible energy transfer pathways is presented in Figure 1(b). The Ni^{2+} absorption band at the 900–1500 nm range is overlapped with the Tm^{3+} absorption band at the 1100–1250 nm range making possibilities of energy transfer between Ni^{2+} and Tm^{3+} .

Figures 2(a)–2(c) show the UC emission spectra of the Tm-only doped and Tm and Ni codoped $\text{CaTi}_{0.9}\text{O}_3$ samples excited at various wavelengths. While excited at the Tm^{3+} absorption bands (1180 and 1660 nm), clear UC emission spectra centered at around 800 nm characteristics of Tm^{3+} ions ($^3\text{H}_4$ to $^3\text{H}_6$ transitions) were observed as shown in Figures 2(a) and 2(b) [11, 14]. Very similar UC emissions were also observed for the Tm and Ni codoped sample while excited at 960, 1300, and 1400 nm (only 960 nm excited UC emission spectrum is shown here, and very similar spectra were observed for all the excitation wavelengths mentioned above) that corresponded to the Ni absorption only (see Figure 1(a)) because no Tm^{3+} absorption bands were located between 850–1100 nm and 1300–1500 nm ranges. This result suggests that under the Ni excitations (960, 1300, and 1400 nm), the incident photons were absorbed by the Ni^{2+} ions, then the energies were transferred to the nearby Tm^{3+} ions, and eventually, Tm^{3+} upconverted at 800 nm. The fact that the Tm-only doped $\text{CaTi}_{0.9}\text{O}_3$ sample did not exhibit such UC emission under 960 nm excitation (Figure 2(c)) confirmed the above mechanism. Figures 2(a) and 2(b) also compare the UC emission intensities for the Tm-only doped

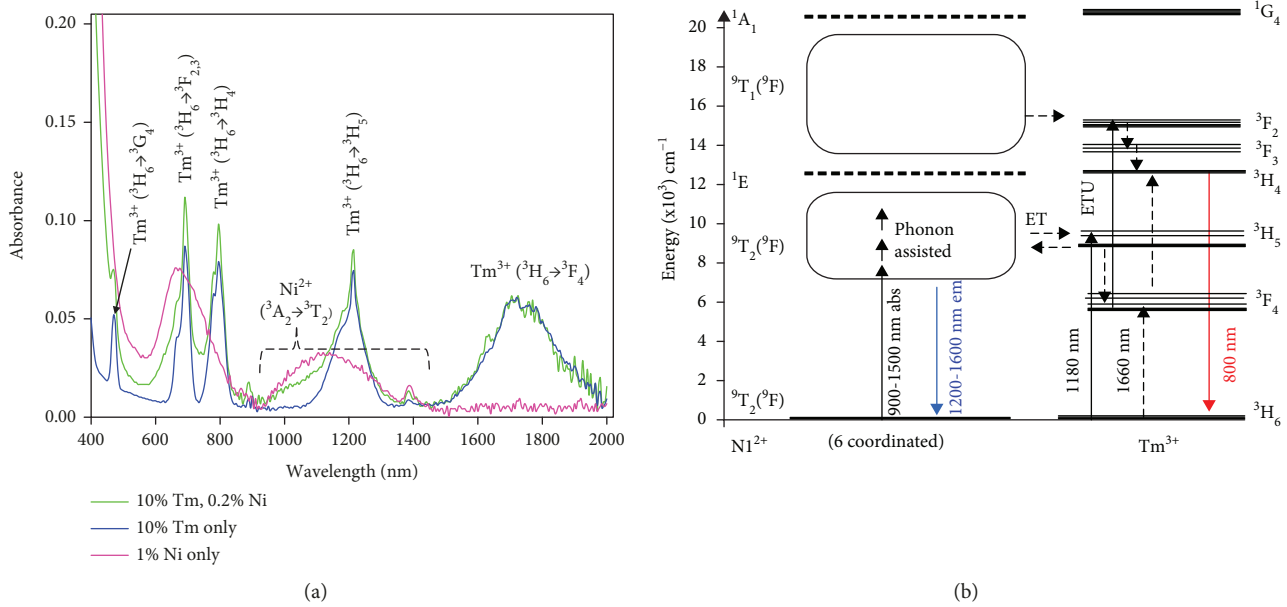


FIGURE 1: (a) Absorption spectra and (b) energy level diagram of the Ni²⁺ and Tm³⁺ ions in the CaTi_{0.9}O₃ host with possible Ni↔Tm energy transfer pathways.

and Tm and Ni codoped CaTi_{0.9}O₃ samples. Under the 1180 nm excitation, the UC emission intensity was reduced by less than 10% suggesting that the back energy transfer from Tm³⁺ to Ni²⁺ and energy dissipation by other Ni-related defects are negligible. On the other hand, for the 1660 nm excitation (Figure 2(b)), UC emission intensity was reduced by more than 60%, suggesting that a large fraction of excited energy dissipated by Ni codoping.

Figure 2(d) shows the excitation power-dependent UC emission intensities while excited at 960, 1300, and 1400 nm (Ni excitation); 1180 nm (both Tm and Ni together excitation); and 1660 nm (Tm-only excitation). The intensity was proportional to the square of the excitation power which confirmed that the UC is a two-photon process under all the excitation wavelengths between 960 and 1660 nm.

The two-photon UC emission mechanism at different excitation wavelengths can be discussed as follows (see Figure 1(b) energy level diagram). Under the 1180 nm excitation, the ³H₅ states get populated through the ³H₆ → ³H₅ transitions within the Tm³⁺ ions. Internal relaxation from the ³H₅ states to the ³F₄ states populates the ³F₄ states. Consecutive excitation by 1180 nm photons populates the ³F₂-excited states (³F₄ → ³F₂). Nonradiative relaxation through the ³F₃ states populates the ³H₄ states. Finally, radiative transition from the ³H₄ states to the ground states (³H₄ → ³H₆) emits 800 nm photons. In a very similar way, under the 1660 nm excitation, the ground state absorption populates the first excited states of the Tm³⁺ ions through the ³H₆ → ³F₄ transitions. Consecutive absorption of the next 1660 nm photons populates the ³H₄ states. Here phonon energy is required to enhance the occupation of the higher energy vibronic levels within the ³F₄ states, because the 1660 nm photon energy is not sufficient for excitation to the ³H₄ levels. One to two phonon energies are enough to assist the excitation under 1600–1700 nm excitation while two to three phonon

energies are required for 1700–1800 nm, considering that the effective phonon energy of the CaTiO₃ host is ~550 cm⁻¹ [15]. Then radiative transitions from the ³H₄ states to the ground states (³H₄ → ³H₆) emit 800 nm photons as in the case of 1180 nm excitations.

For the indirect Ni²⁺ excitation, for example at 960 nm, the exciton photons are absorbed by the Ni²⁺ ions and the ³T₂ states are populated. Phonon-assisted resonant energy transfer from Ni²⁺ (³T₂) to Tm³⁺ (³H₅) followed by internal relaxation (³H₅ → ³F₄) within the Tm³⁺ ions populates the ³F₄ states of Tm³⁺ ions. Consecutive energy transfer from other Ni²⁺ ions to the excited Tm³⁺ ions populate the higher excited states (³F₂) of the Tm³⁺ ions. Here the important point is that the first excited state of Ni²⁺ (³T₂) is quite broad ranging from 900 nm to ~1500 nm. Thermal relaxation to the lowest possible energy state occurs immediately after the excitation. However, due to relatively high effective phonon energy of the CaTiO₃ host (~550 cm⁻¹) [15], occupation probability of the higher energy vibronic states is possible at room temperature. Thus, active phonons assist to transfer the excitation energies in the broad range absorbed by the Ni²⁺ ions to the nearby Tm³⁺ ions at room temperature. For example, when excited at 1490 nm (~0.832 eV), phonon-assisted resonant energy transfer from the ³T₂-excited state (Ni²⁺) to the ³H₅-excited state of Tm³⁺ (0.925 eV; 1340 nm) occurred easily. Here one to two phonon energies (one phonon energy is ~0.07 eV for CaTiO₃ host; ~550 cm⁻¹) are enough to bring the electrons to the resonant level of the ³H₅ states (~0.925 eV) of the Tm³⁺ ions. Up to three phonons assisted energy migration, and UC emission has been well reported in various hosts [16–20]. We observed two photon UC processes in a wide range of excitations from 960 to 1660 nm due to efficient phonon-assisted resonant energy transfer owing to high active phonon energy of the CaTiO₃ host.

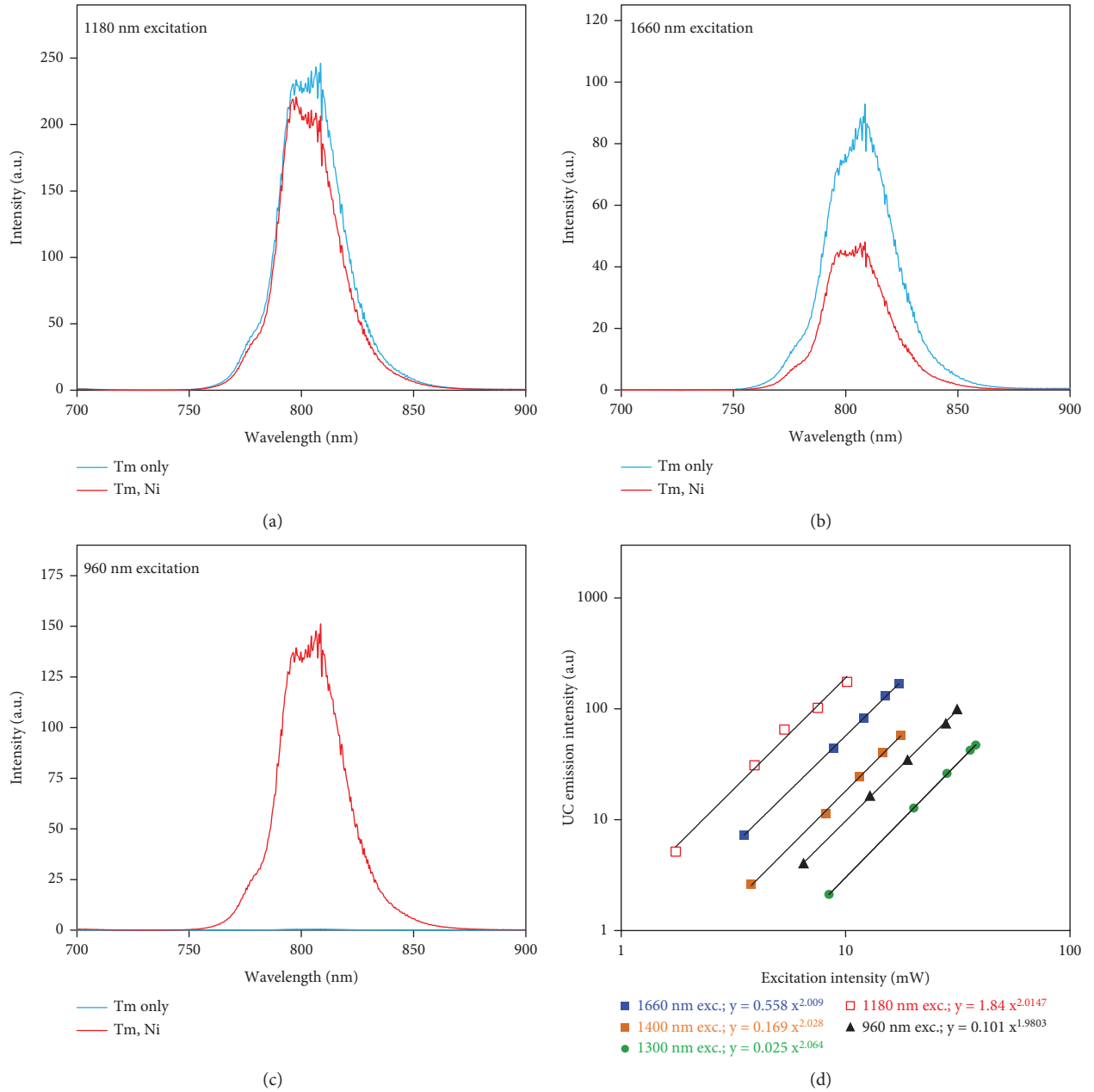


FIGURE 2: UC emission spectra of the Tm-only doped and Tm and Ni codoped $\text{CaTi}_{0.9}\text{O}_3$ samples excited at (a) 1180 nm (both Tm^{3+} and Ni^{2+} absorption), (b) 1660 nm (Tm^{3+} -only absorption), and (c) 960 nm (Ni^{2+} -only absorption). (d) Excitation power-dependent UC emission intensities for the Tm and Ni codoped sample while excited at various wavelengths.

We measured temperature-dependent UC and Stokes emission intensities of the $\text{CaTi}_{0.9}\text{O}_3:\text{Tm}, \text{Ni}$ sample while excited at various wavelengths to support the phonon-assisted energy transfer and UC phenomena, and the results are presented in Figure 3. For 1490 nm excitation, the UC emission intensity at 800 nm gradually increased with increasing temperature. As stated earlier, a fraction of the electrons occupying the higher energy vibronic states within the $^3\text{T}_2$ levels (Ni^{2+}) increases with rising temperature by the host phonon energy assistance. Consequently, phonon-assisted resonant energy transfer from the $^3\text{T}_2$ states (Ni^{2+}) to the $^3\text{H}_5$ states (Tm^{3+}) populates the $^3\text{H}_5$

states efficiently. As a result, population of emitting level increases, and hence, the UC emission intensity of Tm^{3+} also increases with the rise in temperature. Similarly, while excited at 1660 nm, the $^3\text{F}_4$ states of Tm^{3+} get populated. Thermalization relaxes the electrons to the lowest energy levels of $^3\text{F}_4$ states (~ 1900 nm; 0.653 eV). Thus, it is difficult to populate the $^3\text{H}_4$ levels (~ 810 nm; 1.53 eV) by consecutive excitation by other 1660 nm photons (0.75 eV), since the sum of the total energy is only 1.403 eV (0.653 eV + 0.75 eV; 1900 nm and 1660 nm). At increasing temperatures, population of higher energy vibronic levels within the $^3\text{F}_4$ states increases by utilizing two phonon

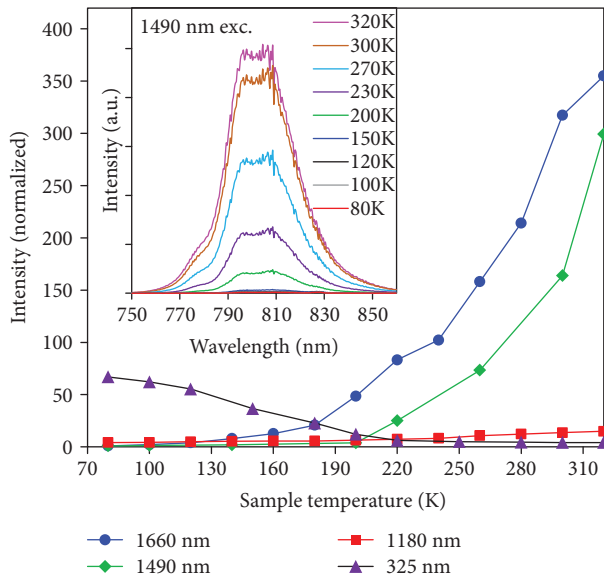


FIGURE 3: Relationship between the sample temperature and UC emission intensities (centered at 800 nm) for the $\text{CaTi}_{0.9}\text{O}_3:\text{Tm}$, Ni sample excited at different wavelengths. Stokes emission intensity while excited at 325 nm is also plotted for comparison. The inset is the typical spectra while excited at 1490 nm.

energies (~ 0.14 eV). Thus, efficient transition from the $^3\text{F}_4$ state to the $^3\text{H}_4$ states occurs (0.653 eV + 0.14 eV by 2 phonons + 0.75 eV by 1660 nm excitation = 1.543 eV; ~ 800 nm) and hence populates the $^3\text{H}_4$ states of Tm^{3+} ions. This results in a more intense UC emission at high temperatures. On the contrary, for the direct Tm^{3+} excitation at 1180 nm, first the $^3\text{H}_5$ states get populated. Internal relaxation ($^3\text{H}_5 \rightarrow ^3\text{F}_4$) populates the $^3\text{F}_4$ states. Thermalization relaxes the electrons to the lowest energy levels of the $^3\text{F}_4$ states (~ 1900 nm; 0.653 eV). Consecutive absorption of the next 1180 nm photons (1.05 eV) easily populates the $^3\text{F}_2$ states (1.70 eV or ~ 730 nm which is equivalent to the sum of 0.653 eV and 1.05 eV). There is no energy mismatch to populate the $^3\text{F}_2$ levels (i.e., $^3\text{F}_4 \rightarrow ^3\text{F}_2$). Thus, the thermal effect on the UC emission intensities is incremental. We further confirmed that if the excitation energy is sufficiently high (325 nm) to ensure host absorption, the Stokes emission intensity at 800 nm monotonically decreased while increasing the sample temperature, which is in accordance with the thermal-quenching behavior.

Figure 4 shows the effect of Tm^{3+} ion concentration on the UC emission intensity excited at 1180 nm. It is clear that the UC emission intensity gradually increased with increasing Tm^{3+} ion concentration up to 10 mol%; above that it decreased. The increased UC intensity was due to increased absorption with increasing Tm^{3+} ion concentration in the CaTiO_3 host as shown in Figure 4(c). Despite the increased absorption, the UC emission intensity decreased at higher Tm^{3+} ion concentrations due to concentration/defect-related quenching where excited electrons relaxed to the ground states nonradiatively. The UC emission intensity also increased with Tm^{3+} ion concentration when excited at the

Ni^{2+} absorption band (1060 nm) as shown in Figure 4(b), although the absorption at 1060 nm remained almost constant owing to the constant Ni^{2+} ion concentration. It is obvious that with increasing the active ion concentration (Tm^{3+} and/or Ni^{2+}), the distance between the Ni^{2+} and Tm^{3+} ions shortened. As a result, energy transfer from the Ni^{2+} (donors) to the Tm^{3+} (acceptors) becomes prominent and increased the UC emission intensity [7, 21].

The $\text{Ni}^{2+} \rightarrow \text{Tm}^{3+}$ energy transfer efficiency was estimated by time-resolved measurements of the Ni^{2+} emission at 1400 nm. Figure 5 depicts the time decay profiles of the Ni^{2+} emissions in the Ni-only doped and Ni and Tm codoped samples when excited at 960 nm (Ni-only excitation). A clear Ni^{2+} emission appeared for the Ni-only doped sample. The lifetime of the Ni^{2+} emission ($^3\text{T}_2 \rightarrow ^3\text{A}_2$) was estimated ~ 0.5 ms. When Tm^{3+} ions were introduced, the Ni^{2+} emission intensity decreased more rapidly indicating the energy transfer from the Ni^{2+} donors to the Tm^{3+} acceptors. The energy transfer efficiency in the Ni and 3 mol% Tm^{3+} codoped sample calculated from the integrated time-dependent intensities of the Ni-only doped and Tm^{3+} codoped samples was 77%; the detail of the procedure is reported in our previous article consisting of the Er and Ni system [9]. When more Tm^{3+} ions were introduced, the energy transfer efficiency further increased and reached 95% at 7 mol% Tm^{3+} . This result confirmed that almost all the energies absorbed by the Ni^{2+} donors were transferred to the Tm^{3+} acceptors at higher Tm^{3+} concentrations. This is the reason why the UC emission intensity increased with Tm^{3+} concentration and even excited under the Ni^{2+} absorption band although the excited light was not absorbed by the Tm^{3+} ions directly. Although slightly increased energy transfer efficiency was realized for the 10 mol% and higher Tm^{3+} doped samples, pronounced $\text{Ni}^{2+} \leftarrow \text{Tm}^{3+}$ back energy transfer and Ni-associated concentration quenching might have reduced the UC emission intensity as in the Ni and Er doped samples [10].

Similarly, the effect of the Ni^{2+} ion concentration on the UC emission intensity of the $\text{CaTi}_{0.9}\text{O}_3:\text{Tm}$, Ni samples excited by 1060 nm was studied by varying the Ni^{2+} ion concentration at a constant Tm^{3+} ion concentration, and the results are presented in Figure 6. With increasing Ni^{2+} ion concentration, absorption at around 900–1200 nm gradually increased and consequently enhanced the UC emission intensity. However, at further higher Ni concentrations, quenching of the UC emission was observed. This might be related to concentration quenching and other defect-related quenching, because defects were pronounced at higher Ni^{2+} doping concentrations as observed in our previous Ca (Ti, Zr) $\text{O}_3:\text{Er}$, Ni upconverters [9, 22]. Thus, the optimum doping concentrations of Tm and Ni in the $\text{CaTi}_{0.9}\text{O}_3$ upconverter to realize intense UC emission were 10 mol% and 0.2 mol%, respectively.

Figure 7 shows the effect of alkali ion substitution on the UC emission intensities for the $\text{CaTi}_{0.9}\text{O}_3:\text{Tm}^{3+}$, Ni^{2+} upconverters when excited at 1060 nm. Substitution of Ca sites with alkali ions in the equivalent amount to that of the Tm^{3+} ions improved the UC emission intensities by at least 2.2 folds, as shown in Figure 7(a). In the $\text{CaTi}_{0.9}\text{O}_3:\text{Tm}^{3+}$,

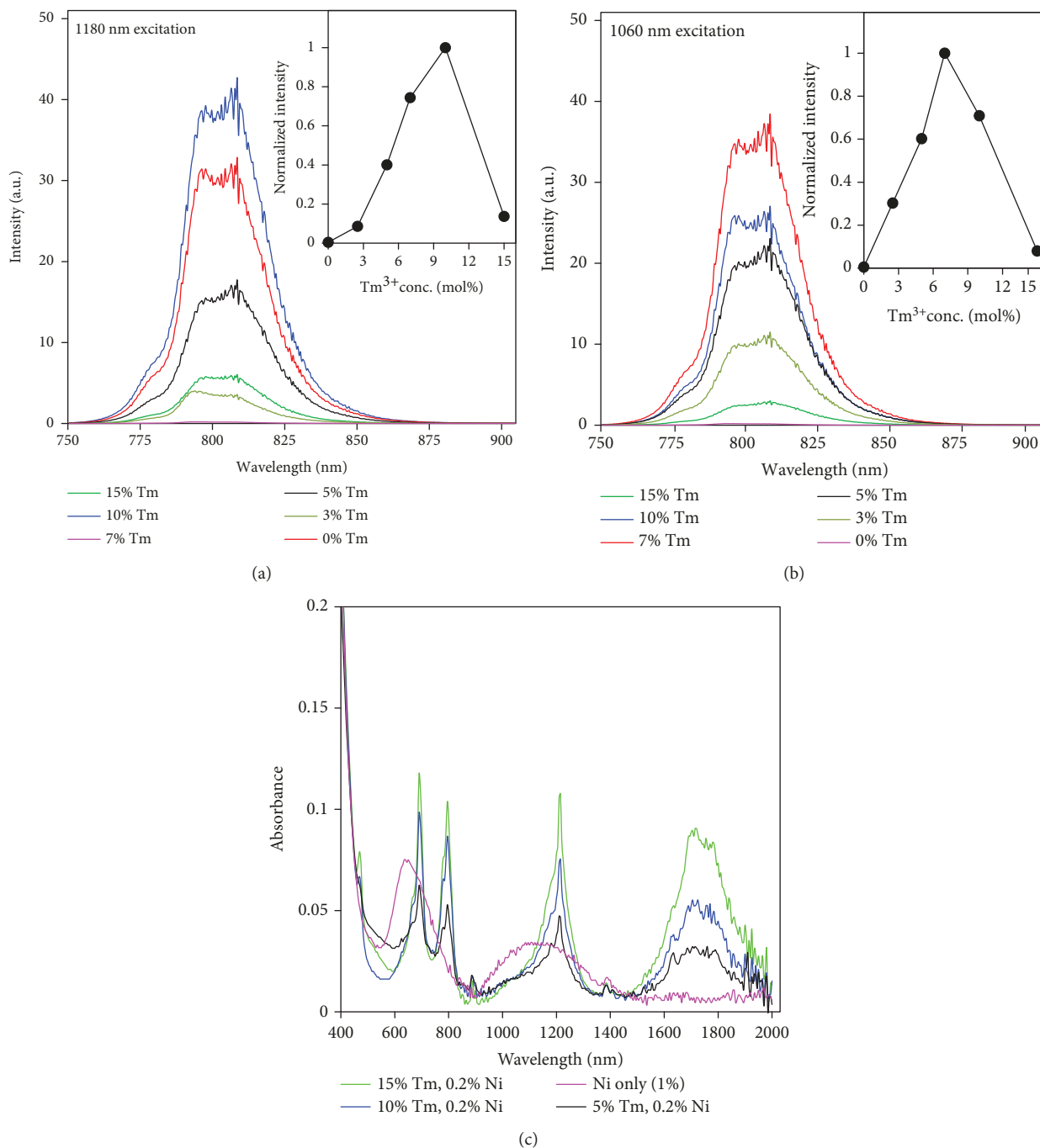


FIGURE 4: UC emission spectra of the $\text{CaTi}_{0.9}\text{O}_3:\text{Tm}, \text{Ni}$ samples with variable Tm^{3+} ion concentrations excited at (a) 1180 nm (both Tm^{3+} and Ni^{2+} absorption) and (b) 1060 nm (Ni^{2+} -only absorption). (c) Absorption spectra of the corresponding samples. Note that the Ni^{2+} concentrations are different in the Ni-only doped and Tm and Ni codoped samples in (c).

Ni^{2+} upconverters, Tm^{3+} ion substitution at the Ca^{2+} sites causes charge imbalance and produces stress which limits the solubility of Tm^{3+} ions into the CaTiO_3 host [12]. Appearance of Tm_2O_3 peaks in the XRD profile of the $\text{CaTi}_{0.9}\text{O}_3:\text{Tm}^{3+}, \text{Ni}^{2+}$ samples (ESI, Figure S2) undoped with alkali ions confirmed lower solubility of rare earth ions into the CaTiO_3 host. Introduction of alkali ions in the equivalent amount compensated the charge imbalance ($\text{Ca}^{2+} + \text{Ca}^{2+} = \text{Tm}^{3+} + \text{Li}^+$), allowing more Tm^{3+} ions to

occupy the Ca sites; as a result, the Tm_2O_3 peaks in the XRD profile disappeared. There was no remarkable difference in the absorption peak positions of the Ni^{2+} and Tm^{3+} ions, but noticeable enhancements of the peak intensities were observed, as shown in Figure 7(b). Obviously, increased absorption improved the UC emission intensities. However, the UC emission intensification was not the same for all the alkali ion substitutions; the order was $\text{Li} > \text{K} > \text{Na} > \text{none}$. It is well known that the $f-f$ transition

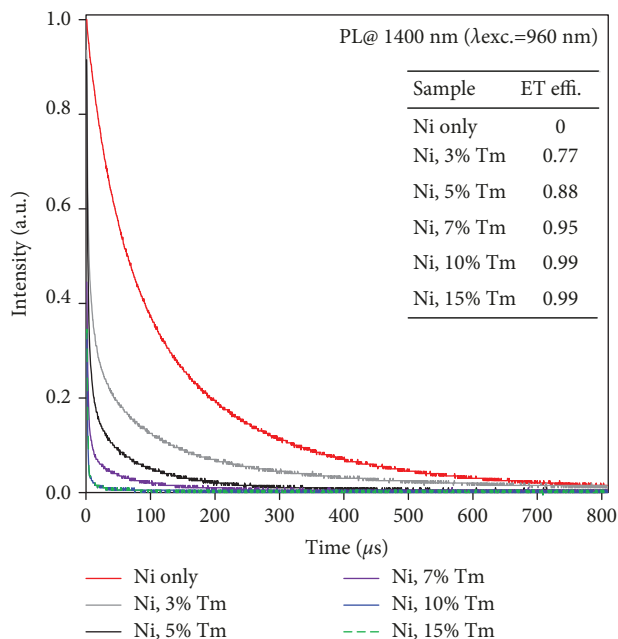


FIGURE 5: Time decay profiles of Ni^{2+} emissions at 1400 nm (± 25 nm) for the $\text{CaTi}_{0.9}\text{O}_3:0.2$ mol% Ni codoped with various concentrations of Tm^{3+} excited at 960 nm (Ni^{2+} excitation).

probabilities of the rare earth ions are partially forbidden in highly symmetrical hosts exhibiting low transition probabilities. As a result, they experience weak absorption and emission intensities in symmetric crystals [22]. Introduction of bigger K^+ ($r_{\text{K}}=0.151$ nm) and smaller Li^+ ($r_{\text{Li}}=0.092$ nm) ions into the CaTiO_3 lattice ($r_{\text{Ca}}=0.112$ nm) deforms the crystal lattice more than the similar-sized Na^+ ($r_{\text{Na}}=0.118$ nm) [23]. As a result, the symmetry around the active ions (Tm^{3+}) is lowered, and the $f-f$ transition probabilities is pronounced [22]. Higher absorption peak intensities in the K^+ and Li^+ ion-substituted samples as shown in Figure 7(b) confirmed this. Since UC is a two-photon process as described earlier, a small increase in the absorption remarkably intensifies the UC emission. Further, due to a smaller Li^+ size and a lower melting point of Li carbonate, it acted as a flux and improved the crystallinity. Increased crystallinity pronounced the UC emission intensity in the Li^+ -substituted samples compared to the K^+ -substituted samples. It has been well reported that bigger K^+ ions form surface defects when heavily substituted, making easier pathways for nonradiative quenching of the excited state electrons, which further decreased the UC emission intensities compared to those of the Li-substituted samples [15].

We have compared the broadband-sensitive UC emission intensities of the $\text{ATiO}_3:\text{Tm}, \text{Ni}$ ($A = \text{Ca}/\text{Sr}/\text{Ba}$) samples to see the effect of the A site cations on the UC intensity, and the results are presented in Figure 8(a). The most intense UC emission was observed for the $\text{CaTiO}_3:\text{Tm}, \text{Ni}$ sample, and the intensity decreased in the order of $\text{SrTiO}_3:\text{Tm}, \text{Ni}$ and $\text{BaTiO}_3:\text{Tm}, \text{Ni}$, in a very similar pattern as in the Er and Ni codoped $\text{AZrO}_3:\text{Er}$ samples reported earlier [8]. It is well reported that CaTiO_3 is composed of the orthorhombic

crystal which is the most distorted structure among the series of ATiO_3 hosts ($A = \text{Ca}/\text{Sr}/\text{Ba}$). The SrTiO_3 and BaTiO_3 are composed of the cubic and tetragonal crystal structures, respectively; see Figure S3 (ESI) [24, 25]. As a result, the A-O bond length and bond angles are more disordered in CaTiO_3 than in $\text{SrTiO}_3/\text{BaTiO}_3$; thus, Tm^{3+} ions experienced the lowest symmetry in the CaTiO_3 host. Since $f-f$ transition of rare earth ions is pronounced dramatically when they experience an asymmetric crystal field as previously stated, the Tm^{3+} ions in the CaTiO_3 exhibited stronger $f-f$ transitions, which was reflected as stronger absorption (Figure 8(b)) and emission intensities. Besides, the UC is a two-photon process, and hence, a small increase in the absorption remarkably increased the UC emission intensity. Thus, the $\text{CaTiO}_3:\text{Tm}, \text{Ni}$ upconverter exhibited the most superior UC performance among the $\text{ATiO}_3:\text{Tm}, \text{Ni}$ ($A = \text{Ca}/\text{Sr}/\text{Ba}$) upconverters.

A very similar result was also observed while the B site cations were varied in the $\text{CaBO}_3:\text{Tm}, \text{Ni}$ ($B = \text{Ti}/\text{Zr}/\text{Hf}$) upconverters as shown in Figure 9. Among these samples, the $\text{CaTiO}_3:\text{Tm}, \text{Ni}$ exhibited the best UC emission performance, and the performance was in the decreasing order for the $\text{CaTiO}_3:\text{Tm}, \text{Ni} > \text{CaZrO}_3:\text{Tm}, \text{Ni} > \text{CaHfO}_3:\text{Tm}, \text{Ni}$ upconverters. In the CaBO_3 ($B = \text{Ti}, \text{Zr},$ and Hf) perovskites, the TiO_6 octahedra is largely twisted to fit in the bigger CaO_8 polyhedra ($r_{\text{Ca}}=0.112$ nm) due to a smaller size of Ti^{4+} ions ($r_{\text{Ti}}=0.06$ nm), whereas the ZrO_6 ($r_{\text{Zr}}=0.072$ nm) and HfO_6 ($r_{\text{Hf}}=0.071$ nm) octahedra get easily fitted. As a result, the CaZrO_3 and CaHfO_3 consisted of a more regular tetragonal crystal structure compared to the more deformed orthorhombic crystal structure in the CaTiO_3 as shown in Figure S4 (ESI) [24, 26]. Thus, transition strengths of the Tm^{3+} and Ni^{2+} ions in the absorption spectra were more pronounced in the CaTiO_3 than in the $\text{Ca}(\text{Zr}/\text{Hf})\text{O}_3$ as shown in Figure 9(b). Besides, the Ni^{2+} absorption and emission band positions red shifted in the CaZrO_3 and CaHfO_3 compounds as shown in Figure 9(b), which increased the $\text{Ni} \leftarrow \text{Tm}$ back energy transfer [8]. As a result, the Tm UC emission intensities further decreased.

Thus, it is concluded that the $\text{CaTiO}_3:\text{Tm}^{3+}, \text{Ni}^{2+}$ was the most efficient broadband-sensitive upconverter among the above studied samples. For this sample, the UC sensitivity, which is defined as the UC emission intensity divided by the square of the absorbed excitation intensity, was calculated and presented in Figure 10. The upconverter developed here exhibited super broadband sensitivity ranging from ~ 950 nm to longer than 1660 nm and can efficiently convert the energies to 800 nm. This upconverter has potential applications for energy harvesting in GaAs, a-Si, $\text{Cu}_2\text{ZnSnS}_4$, and dye-sensitized solar cells whose absorption edges are extended to 800 nm. If 900–1900 nm photons are effectively upconverted to 800 nm photons, the upconverter can contribute ~ 13 mA/cm² current density gain for a single-junction GaAs solar cell. Considering the short circuit current density of ~ 30 mA/cm² and conversion efficiency of $\sim 29\%$ for a present single-junction GaAs solar cell, an improvement in conversion efficiency of $\sim 13\%$ (absolute) is possible [27]. Further, the NIR emission at 800 nm perfectly matches the transparency window

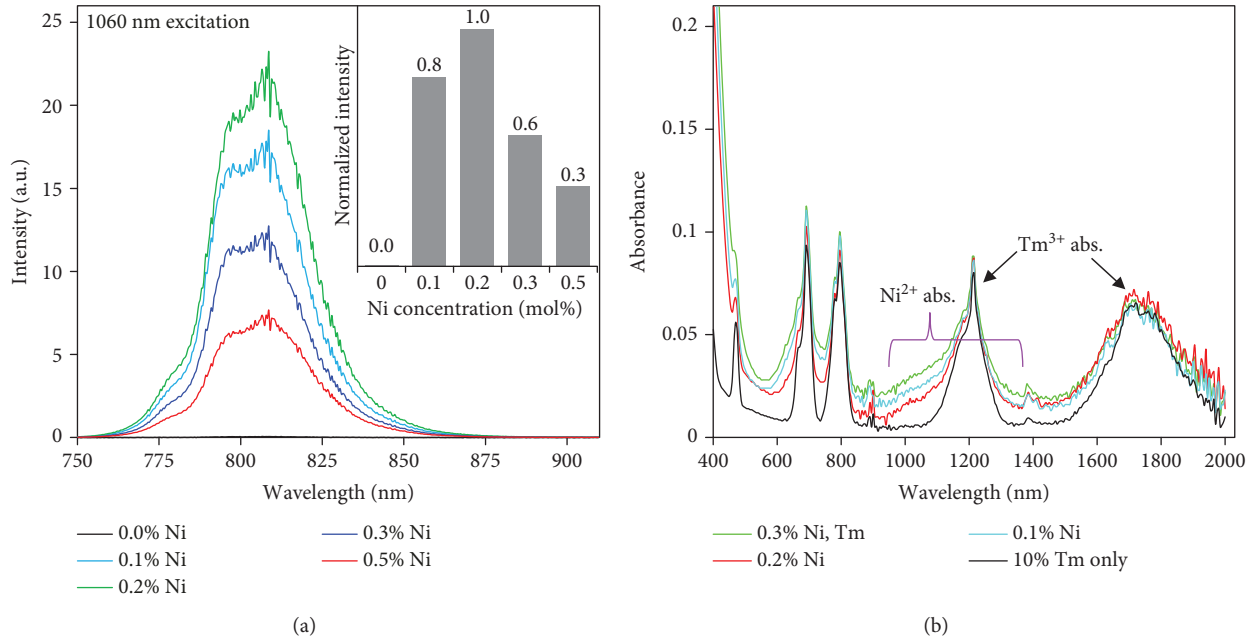


FIGURE 6: (a) UC emission and (b) absorption spectra of the $\text{CaTi}_{0.9}\text{O}_3:10 \text{ mol\% Tm}$ codoped with different Ni^{2+} ion concentrations. The inset in (a) shows the variation of the integrated UC emission intensities with Ni^{2+} ion concentration.

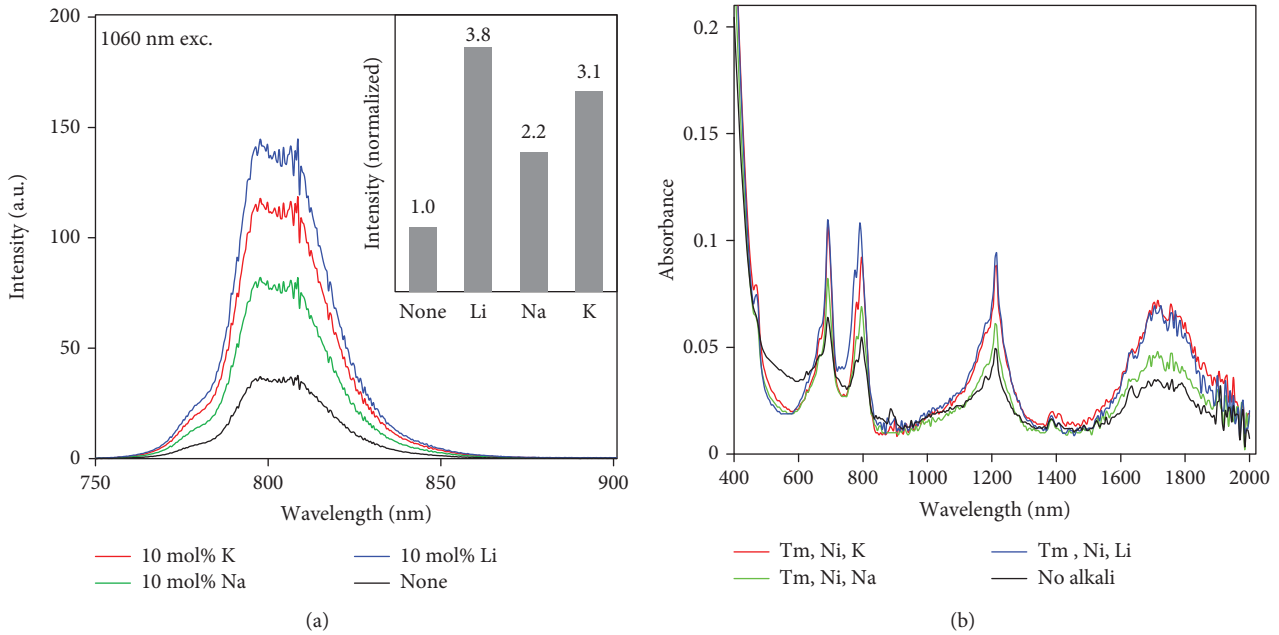


FIGURE 7: (a) UC emission and (b) absorption spectra of the $\text{CaTi}_{0.9}\text{O}_3:\text{Tm, Ni}$ samples codoped with various alkali ions. Inset is the normalized UC emission intensities integrated over 760–860 nm for various alkali ions substitution.

(650–1450 nm) of animal tissues, making the upconverter as a potential candidate for biological imaging besides energy conversion and storage [11]. However, at present, the absorptivity of the developed material is weak, and it should be addressed to utilize super broadband solar radiations efficiently.

4. Conclusions

We have developed a new class of broadband-sensitive upconverters in the Tm and Ni codoped perovskites that absorbs photons in a super broad wavelength range, viz., 900 to ~2000 nm, and emits photons at 800 nm. Six-coordinated

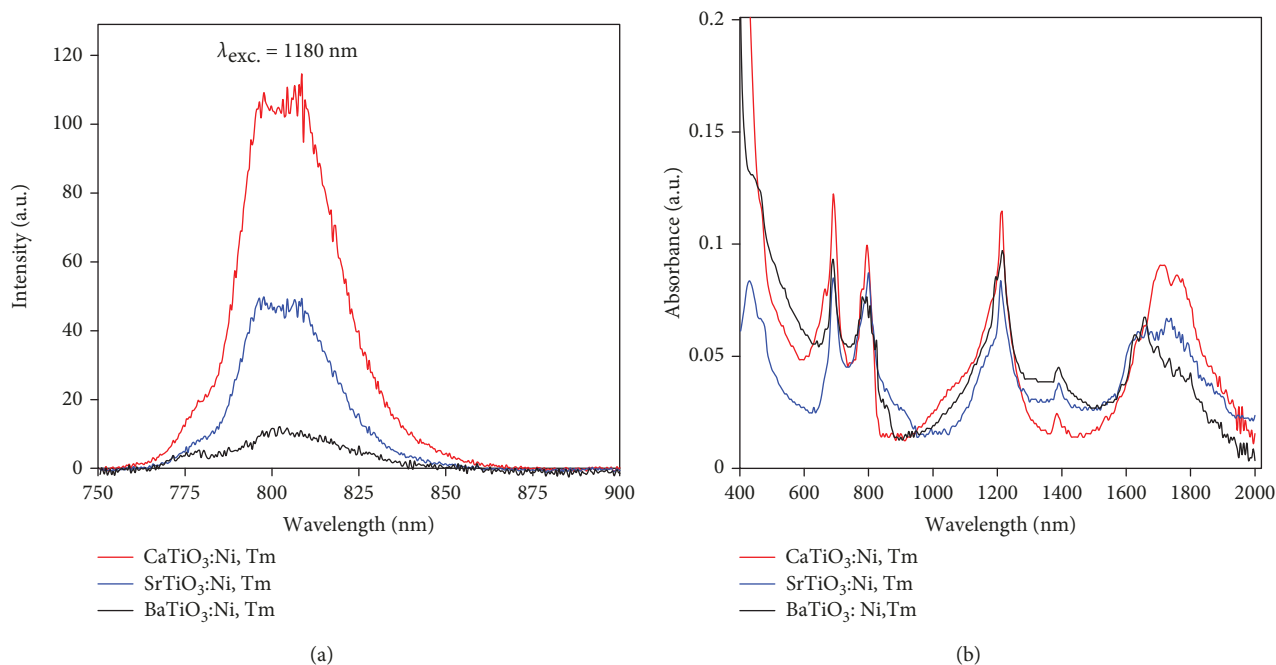


FIGURE 8: (a) UC emission and (b) absorption spectra of the $(\text{Ca/Sr/Ba})\text{Ti}_{0.9}\text{O}_3:10 \text{ mol\% Tm}, 0.2 \text{ mol\% Ni}$ upconverters.

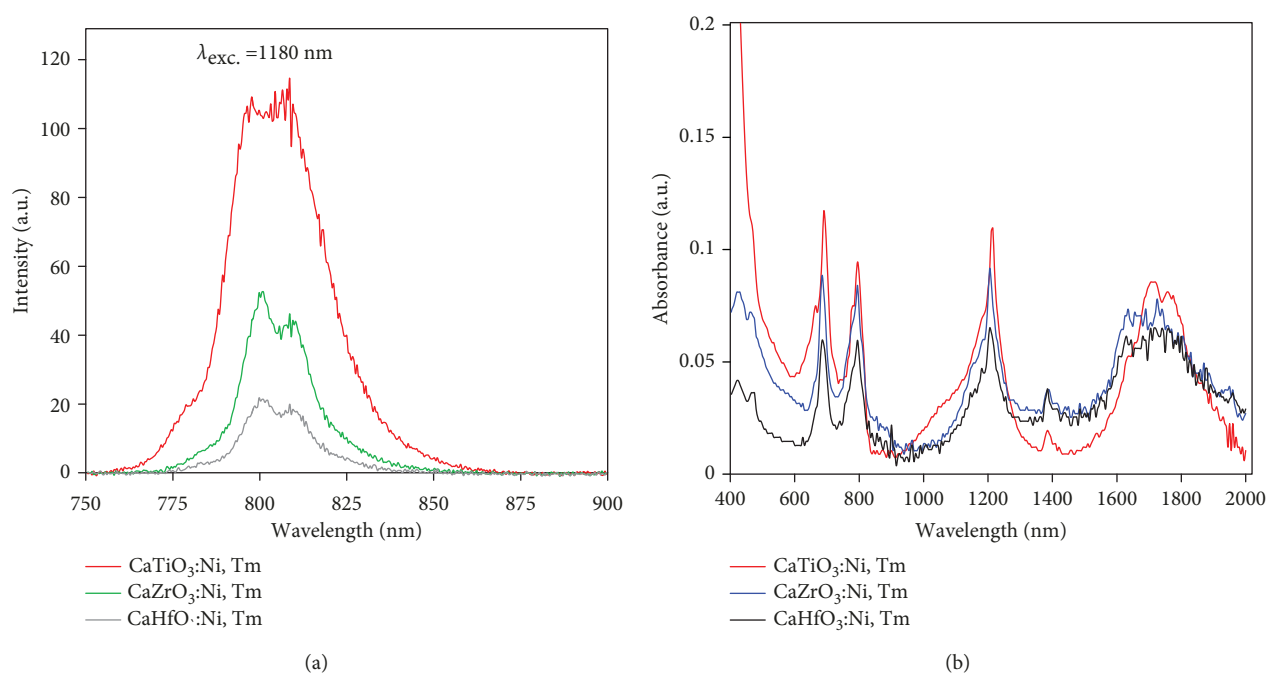


FIGURE 9: (a) UC emission and (b) absorption spectra of the $\text{Ca}(\text{Ti/Zr/Hf})\text{O}_3:10 \text{ mol\% Tm}, 0.2 \text{ mol\% Ni}$ upconverters.

Ni^{2+} ions located at the center of the TiO_6 octahedra (Ti^{4+} sites) absorb 900–1500 nm photons and transfer the energies to the Tm^{3+} ions. In addition to 1100–1250 nm and 1550–2000 nm photons that are directly absorbed by the Tm^{3+} ions, 900–1500 nm photons are also upconverted by the Tm and Ni codoped upconverters. Experimental results suggest that the doping concentration of Tm and Ni for the best UC emission is 10 mol% and 0.2 mol%, respectively. Further, introduction of alkali ions intensified the UC performance by ~5

folds which is due to crystal deformation and balancing of charge during aliovalent substitution. Among the $\text{ABO}_3:\text{Tm}, \text{Ni}$ ($A = \text{Ca/Sr/Ba}$ and $B = \text{Ti/Zr/Hf}$) upconverters, the $\text{CaTiO}_3:\text{Tm}, \text{Ni}$ exhibited the best UC performance due to its unsymmetrical crystal structure. Importantly, the upconverted photons are just below the absorption edges of GaAs, a-Si, $\text{Cu}_2\text{ZnSnS}_4$, and dye-sensitized solar cells, which allow the use of such upconverters in wider solar cell devices. Further, the NIR emission at 800 nm perfectly matches the

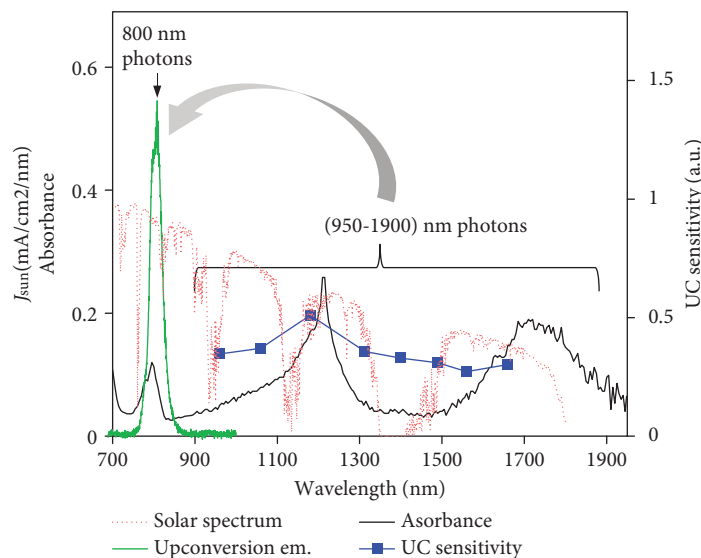


FIGURE 10: Illustration of broadband-sensitive photons UC using the $\text{CaTi}_{0.9}\text{O}_3\text{:Tm, Ni}$ upconverter where photons of solar radiations in the range of 950–1900 nm can be efficiently upconverted to 800 nm photons.

transparency window of the animal tissue and thus possesses potential applications for biological imaging besides energy conversion and storage applications.

Data Availability

All data generated and analyzed during this study are included in this published article and its supplementary information files.

Conflicts of Interest

There are no conflicts of interest to declare.

Acknowledgments

This work was partially supported by the Advanced Low Carbon Technology Research and Development Program (ALCA), Japan Science and Technology Agency.

Supplementary Materials

Figure S1: XRD patterns of the $\text{CaTi}_{0.9}\text{O}_3\text{:Tm, Ni}$ upconverter with variable concentrations of Tm doping. Figure S2: XRD patterns of the $\text{CaTi}_{0.9}\text{O}_3\text{:Tm, Ni}$ upconverter with different alkali ion codoping of the amount equivalent to that of the Tm ions. Figure S3: XRD patterns of the (Ca/Sr/Ba)- $\text{Ti}_{0.9}\text{O}_3\text{:Tm, Ni}$ upconverters exhibiting the orthorhombic, cubic, and tetragonal phases, respectively. Figure S4: XRD patterns of the Ca (Ti/Zr/Hf) $\text{O}_3\text{:Tm, Ni}$ samples exhibiting the orthorhombic crystal phase. (*Supplementary Materials*)

References

- [1] M. A. Green, Y. Hishikawa, W. Warta et al., “Solar cell efficiency tables (version 50),” *Progress in Photovoltaics: Research and Applications*, vol. 25, no. 7, pp. 668–676, 2017.
- [2] F. Auzel, “Upconversion and anti-Stokes processes with f and d ions in solids,” *Chemical Reviews*, vol. 104, no. 1, pp. 139–174, 2004.
- [3] T. Trupke, M. A. Green, and P. Würfel, *Journal of Applied Physics*, vol. 92, no. 7, pp. 4117–4122, 2002.
- [4] S. Fischer, A. Ivaturi, B. Fröhlich et al., “Upconversion silicon solar cell devices for efficient utilization of sub-band-gap photons under concentrated solar radiation,” in *2013 39th IEEE Photovoltaic Specialists Conference (PVSC)*, pp. 3–5, Tampa Bay, FL, USA, 2013.
- [5] R. Martín-Rodríguez, S. Fischer, A. Ivaturi et al., “Highly efficient IR to NIR upconversion in $\text{Gd}_2\text{O}_3\text{:Er}^{3+}$ for photovoltaic applications,” *Chemistry of Materials*, vol. 25, no. 9, pp. 1912–1921, 2013.
- [6] J. C. Goldschmidt and S. Fischer, “Upconversion for photovoltaics - a review of materials, devices and concepts for performance enhancement,” *Advanced Optical Materials*, vol. 3, no. 4, pp. 510–535, 2015.
- [7] Y. Takeda, S. Mizuno, H. N. Luitel, K. I. Yamanaka, and T. Tani, “Energy transfer between Ni^{2+} sensitizers and Er^{3+} emitters in broadband-sensitive upconverters $\text{La}(\text{Ga,Sc,In})\text{O}_3\text{:Er,Ni,Nb}$,” *Journal of Applied Physics*, vol. 120, no. 7, article 073102, 2016.
- [8] H. N. Luitel, S. Mizuno, T. Tani, and Y. Takeda, “Effect of A-site cations on the broadband-sensitive upconversion of $\text{AZrO}_3\text{:Er}^{3+}, \text{Ni}^{2+}$ (A = Ca, Sr, Ba) phosphors,” *Optical Materials*, vol. 64, pp. 314–322, 2017.
- [9] H. N. Luitel, S. Mizuno, T. Tani, and Y. Takeda, “Broadband-sensitive $\text{Ni}^{2+}\text{-Er}^{3+}$ based upconverters for crystalline silicon solar cells,” *RSC Advances*, vol. 6, no. 60, pp. 55499–55506, 2016.
- [10] Y. Takeda, H. N. Luitel, and S. Mizuno, “Competing effects of sensitization and energy dissipation by Ni^{2+} incorporation in $\text{La}(\text{Ga}0.5\text{Sc}0.5)\text{O}_3\text{:Er,Ni,Nb}$ upconverters,” *Journal of Luminescence*, vol. 194, pp. 778–784, 2018.
- [11] H. N. Luitel, R. Chand, H. Hamajima et al., “Highly efficient NIR to NIR upconversion of $\text{ZnMoO}_4\text{:Tm}^{3+}, \text{Yb}^{3+}$ phosphors and their application in biological imaging of deep tumors,”

- Journal of Materials Chemistry B*, vol. 4, no. 37, pp. 6192–6199, 2016.
- [12] H. N. Luitel, S. Mizuno, T. Nonaka, T. Tani, and Y. Takeda, “Effect of Ti compositions for efficiency enhancement of CaTiO₃:Er³⁺,Ni²⁺ broadband-sensitive upconverters,” *RSC Advances*, vol. 7, no. 66, article 41311, 41320 pages, 2017.
- [13] B. Zhou, H. Lin, and E. Y.-B. Pun, “Tm³⁺-doped tellurite glasses for fiber amplifiers in broadband optical communication at 120 μm wavelength region,” *Optics Express*, vol. 18, no. 18, pp. 18805–18810, 2010.
- [14] H. N. Luitel, R. Chand, and T. Watari, “CaMoO₄:RE³⁺, Yb³⁺, M⁺ phosphor with controlled morphology and color tunable upconversion,” *Displays*, vol. 42, pp. 1–8, 2016.
- [15] S. Som, A. K. Kunti, V. Kumar et al., “Defect correlated fluorescent quenching and electron phonon coupling in the spectral transition of Eu³⁺ in CaTiO₃ for red emission in display application,” *Journal of Applied Physics*, vol. 115, no. 19, article 193101, 2014.
- [16] G. Sun, R. Chen, Y. J. Ding, and J. B. Khurgin, “Upconversion due to optical-phonon-assisted anti-Stokes photoluminescence in bulk GaN,” *ACS Photonics*, vol. 2, no. 5, pp. 628–632, 2015.
- [17] K. C. Camargo, R. R. Pereira, L. F. dos Santos, S. R. de Oliveira, R. R. Gonçalves, and L. d. S. Menezes, “Continuous wave near-infrared phonon-assisted upconversion in single Nd³⁺-doped yttria nanoparticles,” *Journal of Luminescence*, vol. 192, pp. 963–968, 2017.
- [18] G. Liu, “Advances in the theoretical understanding of photon upconversion in rare-earth activated nanophosphors,” *Chemical Society Reviews*, vol. 44, no. 6, pp. 1635–1652, 2015.
- [19] Y. V. Orlovskii, R. J. Reeves, R. C. Powell, T. T. Basiev, and K. K. Pukhov, “Multiple-phonon nonradiative relaxation: experimental rates in fluoride crystals doped with Er³⁺ and Nd³⁺ ions and a theoretical model,” *Physical Review B*, vol. 49, no. 6, pp. 3821–3830, 1994.
- [20] J. Su, F. Song, H. Tan et al., “Phonon-assisted mechanisms and concentration dependence of Tm³⁺ blue upconversion luminescence in codoped NaY(WO₄)₂ crystals,” *Journal of Physics D: Applied Physics*, vol. 39, no. 10, pp. 2094–2099, 2006.
- [21] Y. Takeda, S. Mizuno, H. N. Luitel, and K. I. Yamanaka, “Broadband-sensitive cooperative upconversion emission of La(Ga_{0.5}Sc_{0.5})O₃:Er,Ni,Nb,” *Applied Physics Express*, vol. 9, no. 11, article 112402, 2016.
- [22] Q. Huang, H. Yu, E. Ma et al., “Upconversion effective enhancement by producing various coordination surroundings of rare-earth ions,” *Inorganic Chemistry*, vol. 54, no. 6, pp. 2643–2651, 2015.
- [23] <http://abulafia.mt.ic.ac.uk/shannon/ptable.php>.
- [24] “Materials project,” <https://www.materialsproject.org>.
- [25] H. N. Luitel, S. Mizuno, T. Tani, and Y. Takeda, “Broadband-sensitized upconversion of ATiO₃:Er,Ni (A = Mg, Ca, Sr, Ba),” *Journal of the Ceramic Society of Japan*, vol. 125, no. 11, pp. 821–828, 2017.
- [26] E. Pinel, P. Boutinaud, and R. Mahiou, “What makes the luminescence of Pr³⁺ different in CaTiO₃ and CaZrO₃ ?,” *Journal of Alloys and Compounds*, vol. 380, no. 1-2, pp. 225–229, 2004.
- [27] S. Moon, K. Kim, Y. Kim, J. Heo, and J. Lee, “Highly efficient single-junction GaAs thin-film solar cell on flexible substrate,” *Scientific Reports*, vol. 6, no. 1, article 30107, 2016.



Hindawi

Submit your manuscripts at
www.hindawi.com

